

Simulations and model of the nonlinear Richtmyer-Meshkov instability

Guy Dimonte

Los Alamos National Laboratory, Los Alamos, New Mexico 87545

P. Ramaprabhu

University of North Carolina, Charlotte, North Carolina 28223

11/29/09

The nonlinear evolution of the Richtmyer-Meshkov (RM) instability is investigated using numerical simulations with the FLASH code in two-dimensions (2D). The purpose of the simulations is to develop an empirical nonlinear model of the RM instability that is applicable to inertial confinement fusion (ICF) and ejecta formation, namely, at large Atwood number A and scaled initial amplitude kh_0 ($k \equiv$ wavenumber) of the perturbation. The FLASH code is first validated with a variety of RM experiments that evolve well into the nonlinear regime. They reveal that bubbles stagnate when they grow by an increment of $2/k$ and that spikes accelerate for $A > 0.5$ due to higher harmonics that focus them. These results are then compared with a variety of nonlinear models that are based on potential flow. We find that the models agree with simulations for moderate values of $A < 0.9$ and $kh_0 < 1$, but not for the larger values that characterize ICF and ejecta formation. We thus develop a new nonlinear empirical model that captures the simulation results consistent with potential flow for a broader range of A and kh_0 . Our hope is that such empirical models concisely capture the RM simulations and inspire more rigorous solutions.

PACS numbers: 47.20.Bp, 47.25.Jn

1. Introduction

The Richtmyer-Meshkov (RM) instability [1, 2] occurs when a shock encounters interfacial perturbations between two materials of different densities or compressibilities. It is important in inertial confinement fusion (ICF) since several shocks are used to initiate the implosion along a low adiabat. The shocks excite the RM instability at several capsule interfaces which amplify the perturbations that seed the Rayleigh-Taylor (RT) instability [3]. In shock ignition [4], a shock is also launched at the end of the laser drive to ignite the fuel. However, this shock could drive a virulent RM instability because perturbations will have been amplified by previous RM and RT unstable episodes. This could destroy the pusher and modulate the transmitted shock [5]. We believe the RM instability can also produce ejecta [6, 7] from shocked metal surfaces. The evolution of the RM instability is difficult to calculate because of the shock compression, complex material properties and nonlinearities in the late-stages. This can be done with multi-dimensional, high-resolution hydrodynamic simulations but they are computationally intensive and prohibitive for ICF design optimization studies. For such purposes, it is useful to employ reduced 'mix models' [8] that capture the main features of the unstable flows at moderate resolution, but these must be validated using more basic studies.

Eventually, a model of the RM instability must describe how particular broadband initial perturbations grow from the shock impulse and then saturate due to nonlinearities. Unlike the continuously driven RT instability, the RM instability is driven impulsively and may thus be more sensitive to the initial perturbations. In experiments with an unstable impulsive drive [9], the perturbations are found to grow in time as t^θ where $\theta \sim 0.25$ for bubbles and $\theta \sim 0.25 \Rightarrow 1$ for spikes as the density contrast increases. This differs from the $\theta \sim 0.3-0.4$ predicted by bubble merger models [10, 11]. Since such models are based on the nonlinear evolution and interaction of many single modes, the discrepancy in θ may be due to an inadequate description of single modes or the modal interactions. This is complicated by the fact that ICF and ejecta formation operate with an Atwood number near unity, where the models are least accurate.

The single mode evolution of the RM instability has been studied extensively [1-47], yet issues remain. The RM growth rate can be obtained at small amplitude by linearizing the fluid equations [1, 12], but the resulting equations are complex and were first solved numerically. This gave rise to heuristic impulsive models [1, 13, 14] that are easier to evaluate but they have a limited range of accuracy [14, 15]. Analytical solutions [16-19] became available later and have a wider range of applicability. The first experiments [2] obtained growth rates that were smaller than calculated, but this may have been due to nonlinearities (and possibly membranes) since the initial amplitudes were relatively large. Later experiments [20-23] with stronger shocks obtained

good agreement with linear theory at small amplitude. A recent comparison of linear theory, models, experiments and simulations was conducted by Dhotre, Ramaprabhu and Dimonte [24]. The nonlinearities are important [22-46] because they reduce the growth rate relative to the linear rate and they cause the perturbations to grow asymmetrically as bubbles and spikes. At large Atwood number, the bubbles and spikes have quite different asymptotic velocities [34]. Since the full behavior is difficult to describe rigorously, heuristic models [25, 26, 30-33, 36] have been developed to bridge the linear and nonlinear regimes, but they have had only limited success [40, 43, 46]. Unfortunately, they breakdown at large Atwood number and initial amplitude in the regime characteristic of ICF and ejecta formation. In addition, there are compression effects [5, 22, 23, 41, 42] that are fundamental to the RM instability and are difficult to model.

We are interested in investigating these issues in a systematic way by first understanding the nonlinear evolution of a single mode for all Atwood numbers and initial amplitudes. The single-mode behavior is studied here for a variety of conditions using the FLASH hydrodynamics code [47] in two dimensions (2D) since most experiments use 2D perturbations. The results are compared with the experiments and the nonlinear models of Mikaelian [40] (MIK), Zhang and Sohn [25, 26] (ZS) and Sadot, et. al. [30] (SEA) for bubbles and spikes. We find that these models are able to describe the saturation of bubbles and spikes for moderate initial amplitudes and Atwood numbers, but not at the large values encountered in ICF and ejecta production. (Other models [31, 32] were also considered but they work only in the initial stages [43-46].) As a result, we build on the virtues of the previous nonlinear models [25, 26, 30-32, 40] and suggest a new model that agrees with simulations over a wider range of conditions and that recover the asymptotic behavior expected from potential flow models [10, 11, 29, 34, 35]. Such subgrid models are useful for simulations of applications in which interfacial perturbations cannot be resolved.

The paper is organized as follows. In Sec. 2, we describe the configuration and the linear and nonlinear models. The nomenclature is defined here. Our new nonlinear model is summarized by Eqs. 2.24-27 in Sec. 2f. In Sec. 3, we validate the FLASH code using experimental data and make comparisons with the nonlinear models. We summarize our findings in Sec. 4. In the spirit of Richtmyer [1], we develop a simple nonlinear impulsive model in Appendix A to compare with measured growth rates at large initial amplitude.

2. Linear and nonlinear models

The RM instability has been studied extensively in the linear [1, 2, 5, 12-23, 43-45] and non-linear [22-47] regimes and only the salient results are summarized here. Good summaries of the

linear behavior exist [12, 14, 15] and have been updated in Ref. [24]. It is discussed in Sec. 2a because the initial growth rate V_0 determines the early phase and describes most of the compressibility effects. For our purpose, kV_0 sets the time scale for the nonlinear phase, which is assumed to be an incompressible flow since V_0 is usually less than the post-shock sound speeds. In our nomenclature, V is taken to be the growth rate dh/dt with various subscript modifiers, and can be positive or negative as discussed below. Like the early phase, the asymptotic phase is also amenable to analytical treatment as summarized in Sec. 2b. Here, potential flow models [10, 11, 29, 34, 35] obtain an asymptotic growth rate that scales like $1/kt$ for bubbles. The spikes exhibit a more complex behavior [34]. Then, to describe applications, the nonlinear models must bridge the early and asymptotic stages. We describe the models of MIK, ZS and SEA in Secs. 2c, d, and e, respectively, and our new model in Sec. 2f.

We first describe the RM configuration with the aid of Fig. 1. It is adopted from Mikaelian [15] with minor simplifications in nomenclature where noted. The solid horizontal line denotes the interface between ideal fluids A and B which have densities ρ_A and ρ_B and specific heat ratios γ_A and γ_B , respectively. Both fluids begin in pressure equilibrium at p_0 ahead of the shock. A higher pressure p_3 in region 3 produces an incident shock with velocity W_i . By encountering the interface, the shock produces a transmitted shock with velocity W_t into region 0 and a reflected wave with velocity W_r back into region 3. Regions 1 and 2 acquire the same particle velocity (and release pressure) equal to the interface velocity U (Mikaelian uses $u_1 = u_2$ for U). However, they are compressed to different densities ($\rho_B \Rightarrow \rho_1$ and $\rho_A \Rightarrow \rho_2$) such that the pre-shock Atwood number

$$A^- \equiv \frac{\rho_B - \rho_A}{\rho_B + \rho_A} \quad (2.1)$$

changes to a post-shock value of

$$A \equiv \frac{\rho_1 - \rho_2}{\rho_1 + \rho_2} \quad (2.2)$$

The gammas remain γ_B in regions 0 and 1, and γ_A in regions 2 and 3. The post-shock parameters are obtained by solving the transcendental equations distilled from the usual conservation laws, as summarized by Mikaelian [15].

2a. Linear and weakly nonlinear growth rates

For small amplitude, the growth of sinusoidal perturbations can be obtained by linearizing the fluid equations [1, 12, 16-19]. The resulting equations remain complex due to the shock compression and are usually solved numerically. Fraley [16] and Wouchuk [17-19] have obtained approximate analytical solutions. For weak shocks, the main contribution comes from the vorticity deposition from the mis-aligned pressure and density gradients. For strong shocks, there are significant reverberations from refracted sound waves that produce oscillations in the growth rate, but they eventually dampen out. Thus, linear theory predicts that the RM instability has a constant growth rate V_{lin} that applies equally for bubbles and spikes for all time.

To complement analytical solutions, impulsive models [1, 13, 14] were developed to capture the asymptotic RM growth rates for moderate conditions because they are easier to evaluate. For a sinusoidal perturbation of wavelength $\lambda = 2\pi/k$, the pre-shock amplitude h_o^- is reduced by compression to an estimated post-shock amplitude [2] of

$$h_o = h_o^- (1 - U/W_i) \quad (2.3).$$

Then, for $A > 0$, Richtmyer [1] found that the simple model

$$\frac{dh}{dt} = A U k h_o \equiv V_{RM} \quad (2.4)$$

was able to describe the asymptotic growth of his numerical solutions. It was necessary to use the post-shock Atwood number (A) and amplitude (h_o) to capture the shock compression effects.

Using numerical simulations, Meyer and Blewett [13] confirmed Eq. 2.4 but only for $A^- > 0$.

However, for $A^- < 0$, they found that the growth rate depended on the average of the pre- and post-shock amplitudes, namely,

$$\frac{dh}{dt} = A U k \frac{h_o + h_o^-}{2} \equiv V_{MB} \quad (2.5)$$

These so-called impulsive models are useful for their simplicity, but they are accurate only for small compressions [12, 14, 15, 24], namely, when the incident Mach number is near unity or the adiabatic indices are large. They lose accuracy for strong shocks when the densities or adiabatic indices differ substantially.

Another issue is that linear theory is applicable only at small amplitude ($kh_o^- \ll 1$) when the growth rate is small and thus not very important in applications except to seed subsequent RT episodes. Indeed, most RM experiments [2, 20-23, 41-45] have a limited duration and typically use $kh_o^- \sim 0.1-1$ in order to observe significant growth. In such cases, the inferred growth rates are smaller than those predicted by linear theory, possibly because the instability quickly becomes nonlinear. This behavior is observed explicitly in numerical simulations [25-27]. The simulations with $kh_o^- \ll 1$ confirm linear theory but the growth rate diminishes late in time when $kh > 1$. Simulations with $kh_o^- \geq 1$ obtain a growth rate that peaks quickly to a value below that of linear theory and then decays in time. Thus, in most applications, the RM instability is consequential mainly for significant initial amplitudes and this requires a nonlinear treatment.

Nonlinearities can most easily be treated in the incompressible (weak shock) limit by expanding the perturbations in terms of spatial harmonics η_n , each with a time dependent amplitude. The leading harmonics are found to be [25, 26, 29, 31, 32]

$$\eta_1(x, t) = (h_o + V_{lin} t) \cos(kx) \quad (2.6a)$$

$$\eta_2(x, t) = 0.5 A k V_{lin}^2 t^2 \cos(2kx) \quad (2.6b)$$

$$\begin{aligned} \eta_3(x, t) = & -\frac{k^2}{24} \left[(4A^2 + 1) V_{lin}^3 t^3 + 3h_o V_{lin}^2 t^2 + 6h_o^2 V_{lin} t \right] \cos(kx) \\ & + \frac{k^2}{8} \left[(4A^2 - 1) V_{lin}^3 t^3 - 3h_o V_{lin}^2 t^2 \right] \cos(3kx) \end{aligned} \quad (2.6c)$$

where the linear growth rate reduces to $V_{lin} = AUkh_o$ in the incompressible limit since $A \sim A^-$ and $h_o \sim h_o^-$. In the nonlinear regime, it is customary to describe the perturbations as bubbles and spikes. The spikes are centered at $kx = 0$ and the bubbles at $kx = \pi$ for $A > 0$ and vice versa for A

< 0. Then, differentiating Eqs. 2.6 with respect to time and collecting the terms at $kx = 0$ and π , we obtain a spike velocity

$$\frac{V_{sp}}{V_{lin}} = 1 - \left(\frac{kh_o}{2}\right)^2 + \left(A - \frac{kh_o}{2}\right)kV_{lin}t + \frac{4A^2 + 1}{4}(kV_{lin}t)^2 \quad (2.7a)$$

and a bubble velocity

$$\frac{V_{bu}}{V_{lin}} = 1 - \left(\frac{kh_o}{2}\right)^2 - \frac{kh_o}{2}kV_{lin}t + \frac{4A^2 + 1}{4}(kV_{lin}t)^2 \quad (2.7b)$$

Please note that the pre- and post-shock parameters (Atwood number and amplitude) are similar in the incompressible limit. However, their values in Eqs. 2.6 and 2.7 become more ambiguous in the compressible regime.

Equations 2.6 and 2.7 show how the spatial harmonics have a profound effect on the bubble and spike evolution. As expected, their growth rates decrease with kh_o^- even at $t = 0$. This led Velikovich and Dimonte [29] (VD) to obtain a Pade' approximant for the reduction in the initial growth rate with kh_o^- which was found to be in reasonable agreement with data. What is surprising is that Eq. 2.7a predicts that the spike will accelerate for large A. This was indeed observed [24, 30] before the growth rates eventually decayed due to drag effects [10]. According to Eqs. 2.6 and 2.7, the additional nonlinear effects assert themselves when the scaled time

$$\tau_{lin} \equiv k |V_{lin}| t \quad (2.8)$$

exceeds unity as discussed below.

At this point, it is important to clarify the meaning of bubbles and spikes and the sign convention because, unlike the RT instability, the RM growth rate can be positive or negative. As usual, the bubbles (spikes) refer to the penetration of the light (heavy) fluid into the heavy (light) fluid. Their amplitudes (h_{bu} and h_{sp}) are both taken to be $h_o^- > 0$ initially but they can become negative if the perturbations change phase by 180° . This can happen in two ways as seen in the Nova experiments [22, 23]. An immediate sign change can be produced by the shock if $U > W_j$, as indicated by Eq. 2.3. A more gradual sign change occurs if the growth rates (V_{bu} and V_{sp}) are negative such as when $A < 0$. In this case, the magnitude of the perturbation first decreases as it

passes through zero and then increases in the negative (phase shifted) direction. Thus, in the RM instability, it is important to keep track of the sign of the amplitude and growth rate, but the scaled time is always positive as indicated by Eq. 2.8.

In the laboratory frame where $U > 0$, the velocity of bubbles and spikes depend on the sign of A . For $A > 0$, the velocity is $U - V_{sp}$ for spikes and $U + V_{bu}$ for bubbles. For $A < 0$, the velocity is $U + V_{sp}$ for spikes and $U - V_{bu}$ for bubbles.

2b. Asymptotic growth rates

The late stage ($kh \gg 1$) of the RM instability can be described by potential flow models [10, 28, 34] by assuming a quadratic spatial profile around the bubble tip, but they are only strictly valid for $A = 1$. Goncharov [35] and Sohn [37, 38] extended such models to $A < 1$ by ignoring vortical effects and assuming different forms for the velocity potential. They obtain nonlinear differential equations similar to the Bernoulli equation for the amplitude and curvature near the bubble tip. In general, they must be solved numerically although Mikaelian [36] found analytical solutions under limited circumstances.

The models are particularly useful for ascertaining the asymptotic velocities for bubbles (bu) and spikes (sp), which can be written in the form

$$\left| V_{bu/sp}^{\infty} \right| = \frac{1}{F_{bu/sp}(A) k t} \quad (2.9).$$

The scaling of velocity as λ/t was suggested by Alon et al [10] based on simulations and buoyancy-drag considerations. The functions $F_{bu/sp}$ depend on the post-shock Atwood number. In 2D, Oron, et al [11] and Goncharov [35] (OG) obtained

$$F_{bu/sp}^{OG} \Rightarrow 3 \frac{1 \pm |A|}{3 \pm |A|} \quad (2.10)$$

where the upper (lower) sign applies to bubbles (spikes). (In 3D, Goncharov found $F_{bu/sp}^{Gon}(3D) = (1 \pm |A|)/2$.) Sohn obtained a more complex expression (Eq. 19 in ref [38]) for bubbles which reduces to $F_{bu} \sim 1.17$ and 1.67 for $A = 0$ and 1 , respectively, compared to 1 and 1.5 for Eq.

2.10. Thus, the bubble velocity in the Goncharov and Sohn models agree to < 20%, but their bubble curvatures differ by factor of 2.

A critical problem with Eq. 2.9 is that it fails for spikes as $|A| \Rightarrow 1$ since $F_{sp} \Rightarrow 0$. Physically, this reflects the fact that spikes feel no drag when $|A| = 1$ and should simply coast indefinitely. Indeed, Zhang [34] found such an analytic solution

$$V_{sp}^Z = V_o \sqrt{3 \frac{kh_o + 1}{3kh_o + 1}} \quad (2.11)$$

to the potential flow equations for the asymptotic spike velocity at $|A| = 1$. Not only does Eq. 2.11 predict an everlasting spike velocity but it also predicts that the spike will accelerate from V_o to $\sqrt{3} V_o$ at small kh_o , as suggested by the harmonic analysis in Sec. 2a. However, V_o is not specified in Eq. 2.11 and can itself be smaller than V_{lin} at large kh_o , as suggested by VD and discussed further below.

2c. Mikaelian empirical model

To bridge the initial and asymptotic stages, Mikaelian [36, 39] constructed the simplest nonlinear model for a single mode based on analytical solutions he found to the evolutionary equations of potential flow for $A = 1$ [28] and later for all A [35]. Even though the equations are nonlinear, he found the analytical solution

$$h_{bu} = h_o + \frac{1}{F_{bu}^{OG} k} \ln(1 + F_{bu}^{OG} k |V_o| t) \quad (2.12)$$

for the bubble amplitude when $kh_o = 1/3$. The initial growth rate V_o is not specified and can be taken as the linear growth rate V_{lin} . However, ZS discuss how V_o can also be some nonlinear growth rate similar to VD if $kh_o \gg 1$. Differentiating Eq. 2.12 with respect to time gives the bubble growth rate

$$V_{bu}(t) = \frac{V_o}{1 + |V_o|/V_{bu}^\infty} = \frac{V_o}{1 + |V_o| F_{bu}^{OG} k t} \quad (2.13)$$

where the asymptotic bubble velocity is given by the OG model (Eqs. 2.9 and 2.10). Equation 2.13 bridges the initial and asymptotic velocities nicely. For $kh_o < 1/3$, Mikaelian [36] suggests using the linear solution for a time $t^* \equiv (1/3k - h_o)/V_o$ until $kh = 1/3$. Then for $t > t^*$, the nonlinear solution would be given by Eq. 2.12 with a time shift $t \Rightarrow t - t^*$. From Fig. 2 in ref [36], this solution agrees best with 2D numerical simulations for small A and kh_o , but the discrepancies increase with both. This may be due to the fact that Eq. 2.13 (with $F_{bu}^{OG} \Rightarrow F_{sp}^{OG}$) does not describe the spike acceleration suggested by Eqs. 2.9 and 2.10, and as observed by SEA. Furthermore, the analytical solution would not apply for $kh_o > 1/3$ which may occur after re-shocks or previous RT episodes. However, it is still interesting to evaluate Eq. 2.13 as a model for $kh_o > 1/3$ because of its simplicity compared to other models.

2d. Zhang-Sohn empirical model

The ZS model [25, 26] attempts to describe the bubble/spike asymmetry and large initial amplitudes while preserving the nice properties of Eq. 2.12. They start with the harmonic expansion of Eqs. 2.9 and 2.10 that indicate a nonlinear dependence on both kh_o and A , and build a Pade' approximant consisting of the two contributions

$$V_1 \equiv V_o \frac{1}{1 + |kh_o| \tau + \max(0, k^2 h_o^2 + 0.5 - A^2) \tau^2} \quad (2.14a)$$

$$V_2 \equiv V_o \frac{|A| \tau}{1 + 2|kh_o| \tau + 4[k^2 h_o^2 + (1 - A^2)/3] \tau^2} \quad (2.14b).$$

where the scaled time is

$$\tau \equiv k |V_o| t \quad (2.15).$$

Again, the initial velocity V_o is not specified but can be related to V_{lin} . The bubble and spike growth rates are then given by

$$V_{bu/sp}^{ZS} = V_1 m V_2 \quad (2.16)$$

This model is in good agreement with numerical simulations [25, 26, 46] and experiments [43] when compared to the average growth rate for Air-SF6 and Kr-Xe gas mixtures. However, using the average growth rate ignores the contribution of V_2 since it is cancelled out ($V_{bu}^{ZS} + V_{sp}^{ZS} = 2V_1$). This is an important omission since V_2 is required to describe the spike acceleration and the maximum penetration velocity ($U + V_{sp}^{ZS}$) of material for ICF and ejecta applications.

Another important issue with Eqs. 2.14-16 is that they do not reduce to universal asymptotic velocities Eq. 2.9 expected from potential flow theory. For $t \Rightarrow \infty$, their average growth rate reduces to

$$V_1 \Rightarrow V_o \frac{1}{(k^2 h_o^2 + 0.5)\tau^2} \quad (2.17)$$

for $A \sim 0$ and

$$V_1 \Rightarrow V_o \frac{1}{|kh_o|\tau} \quad (2.18)$$

for $A \sim 1$ while the second term reduces to

$$V_2 \Rightarrow V_o \frac{A}{4[k^2 h_o^2 + (1 - A^2)/3]\tau} \quad (2.19)$$

Thus, the asymptotic growth rates become

$$V_{bu/sp}^\infty = m \frac{A}{4[k^2 h_o^2 + (1 - A^2)/3]kt} \quad (2.20)$$

for $A \sim 0$ and

$$V_{bu/sp}^{\infty} = \left[\frac{1}{|kh_o|} \mp \frac{|A|}{4[k^2 h_o^2 + (1-A^2)/3]} \right] \frac{1}{kt} \quad (2.21)$$

for $A \sim 1$. These velocities are $\propto 1/kt$ as expected from potential flow, but the pre-factors are not universal since they depend on A and kh_o , and they can sometimes be negative.

Other models [31, 32] based on different Pade' approximants than ZS agree with experiments [43] and simulations [46] for $\tau < 2-4$, but they diverge later in time.

2e. Sadot et al (SEA) empirical model

The nonlinear model proposed by Sadot, et al (SEA) [30] is based on experiments and numerical simulations, and is designed to capture the asymptotic growth rates expected from the potential flow. They propose the growth rate (Eq. 1 of ref. [30])

$$V_{bu/sp}^{SEA} = V_o \frac{1 + \tau}{1 + (1 \pm |A|)\tau + F_{bu/sp}^{SEA} \tau^2} \quad (2.22)$$

where

$$F_{bu/sp}^{SEA} (|A| \rightarrow 0) = \frac{1 \pm |A|}{1 + |A|} \quad (2.23a)$$

for small $|A| \Rightarrow 0$ and

$$F_{bu/sp}^{SEA} (|A| > 0.5) = 1.5 \frac{1 \pm |A|}{1 + |A|} \quad (2.23b)$$

for large $|A| > 0.5$. The two forms for $F_{bu/sp}$ (Eqs. 2.23) are used so that the asymptotic bubble growth rate reduces to $1/kt$ for $A \sim 0$ and $1/1.5kt$ for $A \sim 1$. For spikes, they expect their model to be accurate only $A < 0.9$.

Equation 2.22 has some benefits and limitations relative to previous models. The two terms $\propto \tau$ are intended to describe the spike acceleration for large $|A|$. For example, as $|A| \Rightarrow 1$ such that $F_{sp}^{SEA} \Rightarrow 0$, the peak spike velocity can exceed V_o since $(1+\tau)/[1+(1-|A|)\tau] > 1$. However, their

spike velocity increases without bound at $|A| = 1$. In addition, Eq. 2.22 does not have an explicit dependence on kh_o , as suggested in Eqs. 2.7 and 2.14. We shall find below that an explicit dependence on kh_o is necessary to describe simulations with large A and kh_o .

2f. New empirical model

The comparisons with experiments and simulations in Sec. 3 will clarify both the virtues and limitations of the aforementioned nonlinear models, particularly as they apply to the extreme conditions of interest, namely, to large $|A|$ and kh_o . For moderate $|A|$ and kh_o , the models obtain good agreement with experiments [30, 43] and simulations [25, 26, 46]. However, the models do not adequately describe the spike acceleration exhibited in the harmonic analysis and simulations. Indeed, the MIK model predicts an immediate reduction in growth rate for both bubbles and spikes. The SEA model describes a spike acceleration by introducing the terms $\propto \tau$, but it fails at large kh_o where simulations and Eq. 2.11 indicate a reduction in spike acceleration. The ZS model could capture this reduction since it depends explicitly on kh_o , but the variation with kh_o is too strong. Our new model builds upon these models to describe simulations relevant to the applications where $|A|$ and kh_o are large.

After many variations, we found that the model

$$V_{bu/sp} = V_o \frac{1 + (1 \mp |A|) \tau}{1 + C_{bu/sp} \tau + (1 \mp |A|) F_{bu/sp} \tau^2} \quad (2.24)$$

is able to describe simulations for a wide variety of $|A|$ and kh_o . The upper (lower) sign applies to the bubble (spike) and, like Eq. 2.10, the scaled time is $\tau = k|V_o|t$. The term $\propto \tau$ in the numerator describes an acceleration mainly for spikes since $1 \mp |A|$ is larger for spikes than bubbles. For intermediate times, this term is balanced by the analogous term $\propto \tau$ in the denominator. The coefficient

$$C_{bu/sp} \equiv \frac{4.5 \pm |A| + (2 \mp |A|) |kh_o|}{4} \quad (2.25)$$

must depend explicitly on kh_o in order to describe the observed reduction in spike acceleration for large kh_o . In simulations, we find that spikes are much more sensitive to kh_o than bubbles and this is described by the $2 \pm |A|$ prefactor. The quadratic term in the denominator is required to obtain asymptotic velocities $\propto 1/kt$ as expected from potential flow. As with previous experiments [43, 45], our simulations (in this paper) are best described with

$$F_{bu/sp} = 1 \pm |A| \quad (2.26)$$

We first tried the OG model (Eq. 2.10) because it was derived from the Bernoulli equation, but it did not fit the simulations as well as Eq. 2.26. For spikes near $|A| = 1$, the 50% difference between Eqs. 2.10 and 2.26 is not important because the τ^2 term is inconsequential since both $F_{sp} \Rightarrow 0$. However, the spike terms $\propto \tau$ make V_{sp} asymptote to $2.3V_{lin}$ when $kh_o \ll 1$ and this is important for ejecta [7]. For bubbles near $|A| = 1$, Eq. 2.26 is 33% larger than Eqs. 2.10 and the asymptotic bubble velocity is in better agreement with simulations, as will be shown in Sec. 3. Similar results were obtained in Refs. [43, 45].

Perhaps a more important parameter in our model is the initial growth rate V_o , which we take to be the same for bubbles and spikes. Remember that V_o contains most of the compressible effects and can be positive (Eq. 2.4) or negative (Eq. 2.5). Since the velocities and kt are both scaled by V_o , it is necessary to determine V_o independently. This is done by plotting kh (which does not depend on V_o) versus τ and adjusting the V_o applied to the simulations for the best fit. For $kh_o \ll 1$, V_o is simply V_{lin} as expected. For $kh_o > 1$, we find that V_o/V_{lin} must be reduced below unity to fit simulations. Our results agree with the Pade' approximant of VD [29], which can be described by

$$V_o = \frac{V_{lin}}{1 + (kh_o^-/3)^{4/3}} \quad (2.27)$$

to within 10%. (Equations 2.7 suggest a simple Pade' approximant of $V_o = V_{lin}/[1+(kh_o/2)^2]$, but this decreases faster with kh_o than our simulations.)

Please note that Eq. 2.27 depends on the pre-shock amplitude since it sets the degree of nonlinearity in the initial growth rate. However, the subsequent flow is best determined by the post-shock amplitude in Eq. 2.25. These points will be discussed further in Sec. 3.

3. Compare simulations, experiments and empirical models

The models are evaluated in this section using existing experimental data and new numerical simulations with the highly validated FLASH code [24, 47]. FLASH is an adaptive-mesh compressible hydrodynamics code that solves Euler's equations using the Piecewise Parabolic Method. This method uses parabolas to interpolate between zones on a Cartesian grid in order to better represent smooth spatial gradients than linear interpolation schemes. A complete description of the code including the results of test calculations are described by Calder *et al.* [47] and references therein. The experiments are those of Dimonte, et al [22, 23] on the Nova laser and Jacobs and Krivets (JK) [43], Sadot, et al [30] on shock tubes and Niederhouse and Jacobs (NJ) [45] on an impulsive experiment. We obtain excellent agreement between the simulations and experiments, but the existing models are only moderately successful. As a result, we propose a new nonlinear model and test all of the models further with new numerical simulations over a wider range of parameters that include those of the applications. With the more complete data set, we can discern both bubbles and spikes with greater clarity and over a longer time than is currently possible experimentally.

Before reporting results, we test our use of the FLASH code for numerical convergence in Fig. 2 with a zoning study of a representative calculation using gamma-law fluids with $A^- = 0.98$, $\gamma_A = \gamma_B = 1.1$. The initial shock has a Mach number of $M_i = 1.02$ and the initial pressure is $p_0 = 1$ bar in the interfacial region. The perturbation has a wavelength $\lambda = 2.09$ cm and initial amplitude $kh_0^- = 1$. The number of zones per wavelength N_λ is indicated for each image and by color in the plot. The results vary mainly as the zoning is increased from $N_\lambda = 8$ to 32. The bubbles vary by 5% in h_{bu} and their symmetry improves. The spikes are poorly defined and off-center with $N_\lambda = 8$ but develop a symmetric head when $N_\lambda = 32$. Their amplitude increases by 15% over this zoning. For $N_\lambda \geq 64$, the results are converged on the wavelength (cm) scale, but, as expected, the small scale features vary significantly. The Kelvin-Helmholtz (KH) features become finer with added resolution and there is some degree of asymmetry. However, h_{bu} and h_{sp} vary by only 2% for N_λ

≥ 64 . As a result of this study, the following simulations are performed with $N_\lambda = 256$ and a 2% estimated numerical uncertainty in h_{bu} and h_{sp} .

3a. Validation with experiments

Here, we use existing experiments not only to test the models but to further validate the FLASH code. The experiments are summarized in Table 1. Even though they were performed in very different venues with weak and strong shocks, they produced similar post-shock Atwood numbers $A \sim 0.6-0.7$ so that the bubble/spike asymmetry is limited. Nevertheless, the experiments are useful for validate the FLASH code, which can then be used to test the models in more detail.

The NOVA experiments [22, 23] were conducted with a target consisting of beryllium (Be) and foam driven by a thermal radiation source. The Be density is less than solid because the Be was evaporated onto a mandrel with machined interfacial perturbations. The shock was essentially infinitely strong ($Mach > 10$) and ionized the solid materials. The velocities and foam density were measured with side-on radiography. The shocked Be density was estimated to be $\rho_2 \sim 2.2$ g/cc based on simulations. The effective gammas were obtained by solving the shock equations [15] and matching the measured W_i/U and W_f/U for a variety of conditions. The pre- and post-shock amplitudes differ in sign because the shock induces a 180° phase inversion since $1-U/W_i \sim -0.4 < 0$. The average scaled (and inverted) RM amplitude $kh \equiv k(h_{bu} + h_{sp})/2$ is represented in Fig. 3 for 2D perturbations. The points were measured with face-on (circles) and side-on (diamonds) xray radiography. As suggested by Eq. 2.15, time is scaled by k and an initial growth rate of $V_o \sim -8$ $\mu\text{m/ns}$ which is in excellent agreement with V_{MB} and 80% of V_{RM} . (Please note that both h_o and V_o are negative.) This is an example of how the MB model is better for $A < 0$ than the RM model. The growth rate decreases for $\tau > 1$ since the nonlinearities assert themselves with $kh > 1$.

The experiments are described very well by a variety of simulation codes with either a radiation drive and a tabular equation of state [23] or a pressure drive and gamma-law fluids [27]. The agreement is excellent not only for the case in Fig. 3, but for wide variety of conditions as seen in Fig. 26 of ref. [23]. The black line in Fig. 3 represents our new calculation with FLASH using the pressure drive with $\gamma_A \sim 1.8$ and $\gamma_B \sim 1.4$. The simulations exhibit the reduction in growth rate beyond $\tau > 1$ and also reveal minor oscillations due to the wave reverberations.

In Fig. 3, the nonlinear models with $A \sim 0.6$ and $kh_0 = 0.26$ are also in excellent agreement with the experiment and simulation. The agreement is impressive since the incident shock is strong and the models are incompressible. This supports the usual hypothesis that the compression effects can be described by V_0 and that the subsequent flow is largely incompressible. In this case, the SEA (green) model obtains the largest amplitude late in time due to the spike acceleration term. Our new model (red) and that of ZS (brown) are smaller due to the explicit dependence on kh_0 . The MIK (blue) model is smaller yet because it does not have any spike acceleration. However, the differences among the models are small because the experimental duration is relatively short ($\tau < 5$).

Relatively longer experiments [30, 43] were conducted on shock tubes using an air \Rightarrow SF₆ combination and weak shocks near Mach ~ 1.3 . The results are summarized in Fig. 4 by plotting the change in scaled average amplitude $kh - kh_0$ vs. scaled time τ . We estimate the grey diamonds from the JK experiments (Fig. 9 of ref. [43]) and the grey circles from the SEA experiments (Fig. 2a of ref. [30]. Please note that our grey circles differ from the points in their Fig. 3a because the author of ref. [30] informed us [48] that their abscissa was actually $A^*\tau$ instead of τ where $A \sim 0.7$.) The JK and SEA experiments are now in excellent agreement with each other and our simulation and model. Our simulation with Mach = 1.3, $A^- = 0.67$, $\gamma_A \sim 1.4$ and $\gamma_B \sim 1.1$ is represented by the black line and open diamonds. We use $kh_0^- = 0.375$ because it lies between the two experimental values 0.26 and 0.47. Our simulation is similar to that of Latini, Schilling and Don [46] (LSD) which is also in excellent agreement with the experiments. The models are evaluated with the post-shock values of $A = 0.71$ and $kh_0 = 0.3$. The SEA (green) model exceeds the experiments and simulations whereas the MIK (blue) and ZS (brown) models are smaller, by an amount of $kh \sim 1-2$ at $\tau \sim 18$. The discrepancy gets worse with time for the ZS model since its growth rate nearly vanishes by $\tau \sim 18$.

The models are tested further by separating the bubbles and spikes, as shown in Fig. 5 for the same conditions in Fig. 4. We plot only the SEA data [30] (grey circles) since the corresponding JK data (Fig. 8 of ref. [43]) has more scatter. As noted by the difference in scales, the bubbles and spikes evolve asymmetrically largely because the bubbles are stagnating for $\tau > 4$ at a value near $kh \sim 2$. The simulation (black line with open diamonds) and most models are in good agreement with the bubble data. The exception is the ZS model because it overestimates the rate at which the bubble stagnates. For the spikes, our simulation and model are in excellent agreement with the experimental results. The SEA model is larger because it overestimates the

spike acceleration for $A \sim 0.7$. The MIK model does not describe spike acceleration and thus underestimates the spike development. The ZS model is again smaller than the data.

The models and simulations are tested further into the nonlinear regime by the incompressible experiments of NJ, as shown in Fig. 6. The NJ experiments were driven impulsively using a coil spring system with a liquid combination ($A^- \sim 0.16$) and small initial perturbations ($kh_o^- = 0.26$). The grey diamonds in Fig. 6 represent the experimental data from Fig. 14 in ref. [45]. The FLASH simulations (black lines and open diamonds) are in excellent agreement with the data. They are performed with $M_i = 1.1$, $A^- = 0.16$, $\gamma_A = \gamma_B = 5/3$ and $kh_o^- = 0.26$. The SEA (green) model overestimates the experiment and simulations because of the term $\propto \tau$ in the numerator and their choice of F_{sp}^{SEA} is too small. Like our model, NJ obtained better agreement in their Figs. 11 and 14 by using $1 \pm |A|$ instead F_{sp}^{SEA} . The difference is 16% for $A = 0.16$. The MIK model is in reasonable agreement with the data even with a large F_{sp}^{SEA} because it lacks the term $\propto \tau$ in the numerator. Our model obtains good agreement even with the term $\propto \tau$ in the numerator because it uses the larger value of $F_{bu/sp}$. The ZS model grossly underestimates the data because it does not capture the asymptotic velocity $\propto 1/kt$ predicted by potential flow models. This experiment is particularly useful because it validates the asymptotic velocity and establishes that $1 \pm |A|$ is a better coefficient than F_{sp}^{SEA} .

These comparisons with experiments are useful because they validate the simulations and models, but they also expose some limitations. There is excellent agreement between experiments and the FLASH simulations and good agreement with the nonlinear models. However, the range of parameters in this comparison is limited even though there were examples with weak and strong shocks. For example, most cases had $A < 0.6$ and $kh_o < 1$ whereas the ICF and ejecta applications can have much larger values for both. In the next section, we will investigate larger values of A and kh_o , and for a longer duration to further differentiate bubbles and spikes.

3b. Compare models with new 2D simulations

Since the FLASH code has been validated here and more extensively for many unstable flows [47], we shall use FLASH simulations to evaluate the nonlinear models more stringently than is currently possible experimentally. In particular, we are interested in conditions that

approximate the ICF and ejecta applications, namely, with $|A| \sim 1$ and $kh_o > 1$. For $|A| \sim 1$, the harmonic analysis and the ZS and SEA models predict that spikes should accelerate in time from their initial (linear) growth rate. This can most easily be seen by plotting the growth rate of the bubbles and spikes separately, and over a long time to ascertain their asymptotic velocities [45]. The numerical simulations have an advantage over experiments because it is easier to take the time derivative of the amplitudes when the measurements are plentiful (every time step). In addition, it is easier to enlarge the computational domain and to vary the fluid characteristics.

A particularly interesting example is shown in Fig. 7 for $A^- = 0.98$, $\gamma_A = \gamma_B = 1.1$ and $kh_o^- = 0.125$. The Mach number = 1.02 is chosen to be near unity to remove any ambiguity in the important scaling factor V_o . In this case, all the growth rates $V_o \sim V_{RM} \sim V_{MB} \sim AUkh_o$ agree to within 9 % because the compression is weak. The bold black lines with open diamonds represent the simulation results. The spike velocity is seen to increase by 60% above its linear growth rate and then decays for $\tau > 1$, but the decay is slow since the upstream fluid is so tenuous. The spike acceleration is attributed to the sharpened profile due to harmonics and it is predicted by the models containing terms $\propto \tau$ in the numerator. However, the peak scaled velocity for spikes is 1.8 and 1.6 for the ZS (brown) and our (red) model, respectively, whereas it is 4.5 for the SEA (green) model. Of course, the SEA model was not intended for $A > 0.9$ and Fig. 7 shows why. The MIK model (blue) shows no spike acceleration because it does not have a term $\propto \tau$ in the numerator. Instead, the MIK spike velocity decays from the start because the denominator asserts itself immediately. The bubble velocity decays immediately in the simulation and in all models but for varying reasons. This is due to a flattening of the bubble profile in the simulations as expected from the harmonics (see Fig. 9). The bubble decays quickly because the term $\propto \tau$ in the numerator is absent in the MIK model and small (0.02τ) in our model. That term is large (τ) for the SEA model but it is normalized by an even larger (2τ) term in the denominator. The ZS model has a negative term $\propto \tau$ in the numerator and thus exaggerates the bubble decay to the point that the bubble amplitude becomes negative. In this case, the ZS and our model agree best with the simulations for spikes whereas all models except the ZS model describe the bubbles.

A very different behavior emerges in Fig. 8 by only changing $kh_o^- = 1$. As expected, the initial growth rate V_o increases nearly eight-fold to a value of $0.95V_{RM}$. In this case, the spike velocity now increases by only 10% and again decays weakly for $\tau > 1$. The bubble evolution is only slightly different than in Fig. 7. Our model (red) obtains such excellent agreement with the simulation that it masks the associated black line and diamonds. Of course, this is done by

construction. The SEA model does not depend explicitly on kh_o and basically repeats its evolution in Fig. 7 with a spike acceleration that is far too strong. In the other extreme, the ZS model depends too strongly on kh_o and grossly underestimates the growth of both bubbles and spikes. The MIK model differs only slightly from Fig. 7 because the nonlinear reduction is applied immediately since $kh_o > 1/3$. Its agreement for bubbles is not surprising since the bubbles depend only weakly on kh_o , but the agreement for spikes is a bit more fortuitous.

The interfacial profiles for the simulations in Figs. 7 and 8 are shown in Fig. 9 at various scaled times. The top two images are for $kh_o^- = 0.125$ and the bottom two are for $kh_o^- = 1$. When $\tau < 1$, the perturbations are symmetric with a nearly sinusoidal profile and grow at a rate close to the linear growth rate. However, for $\tau > 1$, the bubbles have broadened and their growth rate has decreased. Conversely, the spikes have narrowed and have accelerated their growth. This behavior is consistent with the harmonic analysis described in Sec. 2a. As time progresses beyond $\tau \sim 3$, the spike tip becomes multi-valued as the KH roll-ups develop. However, these are not pronounced at this large Atwood number $A^- = 0.98$ and the flow can nearly be described by potential flow. Please note that the perturbations are primarily symmetric in the transverse direction, which indicates that the FLASH code is behaving as expected.

The behavior is easier to understand and more forgiving at small Atwood number, as shown in Figs. 10-12 for $A = 0.15$. We also change $\gamma_A = \gamma_B = 5/3$ to expand our parameter space and keep the Mach = 1.1 near unity to minimize the ambiguity in V_o . Indeed, for $kh_o^- = 0.125$, Fig. 10 shows good agreement between the simulations and all models with $V_o = 1.03V_{RM}$. A different V_o could be applied to the simulations to favor a particular model, but only within a few percent since this is the magnitude of the compressible effects. Essentially, all the calculations show that the bubble and spike growth rates decay from their initial values when $\tau > 1$ in the nearly symmetric manner expected for $A \ll 1$. In Fig. 11 with $kh_o^- = 1$, we obtain good agreement on average between the simulations and the MIK and our models with $V_o = 0.8V_{RM}$ due to the initial nonlinearity. The SEA model exceeds the simulation significantly, although the agreement can be improved by reducing V_o by 40% for the simulations. However, this option is problematic as discussed in connection with Figs. 15 and 20. The ZS model again depends too strongly on kh_o and grossly under-estimates both bubbles and spikes.

Sample profiles of the interfacial perturbations are shown in Fig. 12 for the cases in Fig. 10 and 11. As before, the top two images are for $kh_o^- = 0.125$ and the bottom two are for $kh_o^- = 1$. Since $A^- = 0.15$ is small, the perturbations remain symmetric well into the nonlinear regime $\tau \gg 1$ as expected. In addition, the KH roll-ups are pronounced and exhibit a cascade to smaller scales as they breakup due to the unstable shear flow.

The comparisons in Figs. 5-11 show that nonlinear models of varying complexity are able to describe RM bubbles and spikes, but only under limited circumstances. Our new empirical model is constructed to expand the range of validity to include the ICF and ejecta applications. This requires that the model is accurate over a wide range of A and kh_o^- . This will be shown in the following.

A key set of simulations for developing our empirical model is summarized in Fig. 13 in which we vary A^- . The simulations are performed with $\gamma_A = \gamma_B = 1.1$ and are represented by solid lines of different colors for $A^- = 0.98, 0.94, 0.88, 0.75, 0.5$ and 0.25 . By construction, our model (dashed lines of corresponding color) is in excellent agreement for all A^- . The initial amplitude $kh_o^- = 0.125$ and Mach = 1.02 are small to minimize the ambiguity in V_o . Indeed, the value of V_o applied to the simulation results is always within 7 % of V_{RM} . The key simulation results for model development are as follows. For large $|A|$, the spike velocity (Fig. 13a) increases from its initial value to a peak value that increases with $|A|$, and then decays asymptotically. The initial increase is described by the interplay between the two terms $\propto \tau$, which by themselves approach $(1+|A|)/C_{sp} > 1$ for $kh_o^- \ll 1$. However for $|A| \neq 1$, the τ^2 term eventually dominates and the spike velocity decays asymptotically. This does not occur at $|A| = 1$ and the spike remains at the enhanced value as calculated by Zhang [34]. The bubble velocity (Fig. 13b) is not enhanced and decays immediately for all A since $(1-|A|)/C_{bu} > 1$. However, in contrast to the spikes, the bubble velocity decays more rapidly as A increases. Physically, these characteristics can be traced to the contributions of the spatial harmonics at large amplitude, and this is observed in the simulations.

It is possible to compare all models with these simulations compactly by simply evaluating the peak scaled spike velocity at various A , as shown in Fig. 14, with $kh_o^- = 0.125 \sim kh_o^-$. Our simulations (black line plus diamonds) exhibit no spike acceleration for $A < 0.5$ and increase to $V_{max} V_o \sim 1.65$ at $A = 0.98$. This compares well with the value of 1.57 from Eq. 2.11 with $kh_o^- = 0.125$, as predicted by Zhang [34] for $A = 1$. Our model (red) is in excellent agreement with the simulations for $A \leq 0.98$ and approaches $2/C_{sp} = 2.06$ at $A = 1$. The ZS (brown) model obtains

slightly larger peak velocities than the simulations whereas the SEA (green) model greatly exceeds the simulations. Of course, the MIK model has no spike acceleration and remains at the initial value of V_o .

Another key set of simulations for model development involves the variation with kh_o^- , as shown in Fig. 15, at $A^- = 0.98$ and $\gamma_A = \gamma_B = 1.1$. The simulations (solid lines of different color) are performed with $kh_o^- = 0.125, 0.25, 0.5, 1, 2, \text{ and } 4$. Again, $M = 1.02$ is kept small to minimize compression effects so that $A^- \sim A$ and $kh_o^- \sim kh_o$. By construction, our empirical model (dashed lines with same colors) fits the simulations very well. However, to describe the decline in the spike acceleration with kh_o in Fig. 15a while maintaining the agreement with the variation in A , it is necessary for V_o to decrease with kh_o . This is expected from the harmonic analysis (Eq. 2.7) and we find that V_o can be related to the linear growth rate V_{lin} by the Pade' approximant of VD [29]. If a smaller value of V_o were used, the scaled bubble velocity would exceed unity and violate the simulations. (Please note that the code values of V_{sp}/V_o do not approach unity as $\tau \Rightarrow 1$ when $kh_o^- > 2$ because we have had to time average the $h_{sp}(t)$ in order to take its derivative. However, this has little effect in Figs. 15c and d where the agreement is excellent.) Our use of the VD scaling coupled with our choice of $C_{bu/sp}$ is key for obtaining good agreement for both bubbles and spikes. In particular, our simulations show that the spikes are very sensitive to kh_o whereas the bubbles are not. This qualitative difference between bubbles and spikes can only be described by having $V_{bu/sp}$ and V_o depend explicitly on kh_o (as suggested by VD).

The peak scaled spike velocity from the models are compared in Fig. 16 as a function of kh_o for the conditions in Fig. 15. The simulations (black line plus diamonds) indicate that the spike acceleration relative to V_o occurs only for small kh_o . Again, our model (red) is in excellent agreement with the simulations. The dashed magenta line represents the theory of Zhang [34] (Eq. 2.11) for $A \Rightarrow 1$ and it agrees within 15% with our simulations and model. The ZS model (brown) is smaller than observed for $0.2 < kh_o < 2$ and larger for $kh_o < 0.2$. The MIK and SEA models do not depend explicitly on kh_o and are fixed at $V_{max}/V_o = 1$ and 4.25 , respectively, at $A = 0.98$.

For completeness, the variation of the bubbles and spikes with kh_o at small $A^- = 0.15$ is shown in Fig. 17. Again, the simulations (solid lines) are performed with $\gamma_A = \gamma_B = 1.1$ and $kh_o^- = 0.125, 0.25, 0.5, 1, 2,$ and 4 . The Mach = 1.02 is kept small to minimize compression effects so that $A^- \sim A$ and $kh_o^- \sim kh_o$. As before, the simulation results are scaled by a V_o that relates to the linear growth rate according the VD Pade' approximant [29]. Our model (dashed lines) agrees with this prescription. Basically, at small A , the scaled spike and bubble velocities decay more quickly with kh_o but only weakly.

Finally, it is possible to evaluate the $F_{bu/sp}$ term by investigating the asymptotic velocities from simulations of long duration. Figures 18 and 19 show the scaled velocities for bubbles and spikes, respectively, for the four conditions summarized in Table 2. We set $kh_o^- = 1.0$ to obtain appreciable growth during the simulation, but the dependence on V_o cancels out late in time. For example, our model reduces to

$$V_{bu/sp} \Rightarrow \frac{V_o}{F_{bu/sp} \tau} = \frac{1}{F_{bu/sp} k t} \quad (3.1)$$

asymptotically for $|A| \neq 1$. The asymptotic behavior of the other models is also independent of V_o , as described in Sec. 2. For bubbles, the simulations (black solid lines) in Fig. 18 do indeed exhibit the $1/kt$ scaling represented by the slope of the dashed lines. The ZS (brown) model does not exhibit the expected scaling because it involves the difference of two terms and can become negative. The other models show the expected scaling but the OG factor is too small at large A so that the asymptotic velocities are too large. In particular, for $A = 0.98$, the bubble velocity for the MIK (blue) and SEA (green) models exceed that of the simulation (black) because $F_{bu}^{OG} \sim 1.51$. Our model is made to fit the simulations better by choosing $F_{bu} = 1+|A| = 1.98$. Of course, this distinction is reduced as A decreases since $1+|A|$ and F_{bu}^{OG} approach unity at $A = 0$. However, the SEA model has $F_{bu}^{SEA} = 1$ for all $A \leq 0.5$, which is smaller than $1+|A|$. This is a contributing factor to the large velocities obtained from the SEA model in Figs. 18a and b.

The spikes behave differently, as shown in Fig. 19 for the same conditions in Fig. 18. They achieve the $1/kt$ velocity only at small A where they are similar to bubbles. However, as $|A|$ approaches 1, the spike velocity deviates from the $1/kt$ scaling represented by the dashed lines. This is reasonable since the spikes go through an acceleration phase at large A and actually

approach a velocity that exceeds V_o as predicted by Zhang [34] at $A = 1$. Our model (red) reproduces the simulations (black) for all A , thereby validating our time dependence and choice of F_{sp} . The MIK (blue) model has the next best agreement but this is somewhat fortuitous because our simulations have $kh_o^- = 1$. The MIK model is insensitive to kh_o^- whereas the simulations vary substantially with kh_o^- , as seen in Figs. 7-8a. The spike velocity is underestimated by the ZS (brown) model and overestimated by the SEA (green) model. These results show that the asymptotic spike velocities are not universal and cannot be obtained by simply changing the sign of A in potential flow models [10, 35] for bubbles.

3c. V_o and large amplitude experiments

Our empirical model shows excellent agreement over a wider range of parameters than previous nonlinear models because it is based on two components. The first component depends explicitly on A and kh_o as described by Eqs. 2.24-27. It is meant to capture the largely incompressible flow following the initial impulse V_o . However, as in all such models, V_o is not specified. Our second component involves the realization that V_o itself decreases with kh_o and our reduction factor is consistent with the VD Pade' approximant [29]. This demonstrated in Fig. 20 for all of our simulations (diamonds) over a variety of conditions ($Mach$, A^- , γ_A , γ_B , kh_o^-). The linear growth rate V_{lin} is defined by the observed initial growth in our simulations at $kh_o^- = 0.125$ and is meant to capture most of the compressible effects. An exhaustive comparison of simulations with analytical solutions and impulsive models is described previously [24]. In our case, V_o is determined by fitting the scaled average amplitude kh from our simulations to that in our model. The Pade' approximant of VD (solid line) agrees with the simulation results within 10-15%. The dashed line in Fig. 20 represents Eq. 2.28, which agrees with the VD approximant to within a few percent but has a simpler form.

In the beginning of our study, we tried to fit the established models to our numerical simulations by only adjusting V_o/V_{lin} for each case. This yields a different dependence of V_o/V_{lin} on kh_o^- . This was successful at small A where the bubbles and spikes are similar, but not at large A where the spikes are very sensitive to kh_o^- and the bubbles are not. For example, in Fig. 11 for $A^- = 0.15$, the simulations would better fit the SEA model if V_o was reduced by 40 %. However,

such an adjustment would not be successful at large A (Figs. 7, 8, 13, 15) where the behavior for bubbles and spikes is dramatically different.

As mentioned previously, many RM experiments used large initial amplitudes in order to observe significant growth and their results can also be explained by our model. In experiments, the initial growth rate is inferred by fitting a straight line to measurements of the peak-to-valley amplitude (divided by 2) at various times. This is usually done in a time period during which the amplitude increases by some fraction of a wavelength. When compared to the expected linear growth rate, the experiments [20-23, 41] find that growth rate decreases with kh_o^- as indicated by the points in Fig. 21. The solid black line represents the initial growth rate (Eq. 2.27) at $t = 0$. This is just the upper limit for the growth rate since the experimental observation only begins at $t = 0$. The observation occurs over a finite time during which the growth rate decreases due to additional nonlinearity. A lower limit to the growth rate can be estimated by our model

$$\frac{V_{\text{exp}}}{V_{\text{lin}}} = \frac{1}{2} \left\{ \frac{2 - |A|}{2 - A^2 + (4.5 + |A| + (2 - |A|)kh_o^-)/4} + \frac{2 + |A|}{2 - A^2 + (4.5 - |A| + (2 + |A|)kh_o^-)/4} \right\} \tag{3.2}$$

$$* \left\{ \frac{1}{1 + (kh_o^-/3)^{4/3}} \right\}$$

evaluated at $\tau = 1$ since the amplitude has increased by $\sim 1/k$ by this time. The two terms in the first bracket are the bubble and spike growth rates, respectively, at $\tau = 1$, and they depend on the post-shock amplitude. The second bracket contains the initial reduction factor and it depends on the pre-shock amplitude. The dashed (dotted) line represents Eq. 3.2 at $A = 1$ (0) assuming no shock compression, namely, with $kh_o = kh_o^-$. It can be seen that the experimental points lie between our model results at $\tau = 0$ and 1. This is reasonable since the measurements are typically fitted over such a time scale.

The red line in Fig. 21 represents our nonlinear impulsive model obtained in Appendix A in the spirit of Richtmyer. We re-write the model (Eq. A.3) as

$$\frac{1}{V_{\text{lin}}} \left(\frac{dh}{dt} \right)_o = \frac{(kh_o^- - 1) + \sqrt{(kh_o^- - 1)^2 + 8(kh_o^-)^2}}{4(kh_o^-)^2} \tag{3.3}$$

in order to apply the model to the data for all A and compressions. In other words, in Eq. A.3, we interpret V_0 as the linear growth rate V_{lin} and the initial growth rate $(dh/dt)_0$ as measured over a small but finite time in an experiment or simulation. We also believe that the initial amplitude should be the pre-shock amplitude because it establishes the degree of nonlinearity prior to compression. The agreement between the data and our nonlinear impulsive model is surprising yet interesting because it captures some essential features. For $kh_0^- \ll 1$, the model reduces to the linear growth rate as it should. The small increase kh_0^- with above unity may be accidental or it may reflect the spike acceleration at large A . Then, for $kh_0^- \gg 1$, Eq. 3.3 is proportional to $1/kh_0^-$ such that the growth rate saturates at $\propto A*U$ since the linear growth rate is $\propto kh_0^-$. Such behavior is suggested by our simulations, but further investigation is required.

4. Summary and discussion

We have conducted many simulations with the FLASH code to investigate the RM instability over a wide range of conditions including those relevant to applications like ICF and ejecta formation. The FLASH code was used to expand the parameter regime (M_i , A^- , γ_A , γ_B) beyond that available experimentally. However, we did use available experimental data on a variety of platforms to validate the FLASH code for RM flows. FLASH has also been validated for different flows [47] and compared with other codes [27]. In addition to a wider parameter range, the simulations provide more complete diagnostic clarity. The simulations reveal that bubbles stagnate when they grow by an increment of $2/k$ and that spikes accelerate for $A > 0.5$ due to higher harmonics that focus them.

In order to capture the simulation results quantitatively, we compared the linear evolution with theory and impulsive models [24] and the late-time behavior with empirical models [25, 26, 30-33]. At small amplitude, we obtain excellent agreement between our simulations and linear theory, which increases our confidence in FLASH. At the same time, we confirm the expected result that the impulsive models are accurate only in limited regimes, although they are attractive intuitively. However, since the RM growth rate increases with the initial amplitude, the RM instability is of consequence in applications mainly when the amplitude is large and impacted by nonlinear effects. Since rigorous nonlinear theories are limited, we examined the empirical models of MIK, SEA and ZS that bridge the initial and asymptotic evolution. We found that they agree with the simulations for moderate values of the Atwood number and amplitude. However, they do not agree for the large values of $A^- > 0.9$ and $kh_0^- > 1$ that occur in the

applications like ICF and ejecta formation. To extend to these important applications, we developed the empirical model described in Sec. 2f.

Before describing the virtues and limitations of the empirical models, we first summarize our simulation results. At small Atwood number, the bubbles and spikes evolve similarly. For $kh_o^- \ll 1$, they grow initially with the linear growth rate and then transition to the asymptotic velocity $\propto \lambda/t$ expected from potential flow. For large initial amplitude, the initial growth rate is smaller than that given by linear theory in agreement with the Pade' approximant described by VD [29]. However, the asymptotic growth rate is similar. At large Atwood number, the bubble evolution is similar to that at small A^- but the spike evolution is quite different. For small initial amplitude, the spike velocity begins at the linear growth rate and then increases as though it is being accelerated. Physically, this can be traced to the spatial harmonics that develop in the initial nonlinear regime which focus the spikes and broaden (and retard) the bubbles. As time evolves further, the spike velocity decreases due to the drag from the downstream fluid. However, at $A^- = 1$, the drag is absent and the spike velocity remains at an elevated stage consistent with the theory of Zhang [34]. Our simulations and Zhang's theory show that this maximum spike velocity decreases with the initial amplitude. The bubble growth is consistent with conventional wisdom, namely, that it transitions in some universal way from the initial growth rate to an asymptotic velocity $\propto \lambda/t$. However, at large A^- , the spikes evolve in a complex manner since they are first accelerated and then reach an asymptotic velocity which depends on both A^- and kh_o^- .

Some of this behavior is captured by the existing empirical models of MIK, SEA and ZS, but they are quantitatively accurate only for limited conditions. The MIK model simply makes a transition from the initial to asymptotic growth rates and the bubble and spike asymmetry is captured by the function $F_{bu/sp}$. It works well at small A^- but does not describe the spike acceleration at all. The SEA model is based on experiments and simulations for $A^- < 0.9$ and does exhibit the spike acceleration. However, it breaks down at large A^- and kh_o^- (where applications occur) because it overestimates both the magnitude and dependence on kh_o^- of the spike acceleration. The ZS model is based on Pade' approximants of the harmonic analysis and does exhibit the spike acceleration and has an explicit dependence on kh_o^- , unlike the SEA model. However, the particular Pade' approximation often produces strange behavior such as

sign reversals. These models agree with simulations for moderate A^- and kh_o^- but not for the large values relevant to the applications.

To be accurate for the large values of A^- and kh_o^- in the applications, we had to develop a new empirical model given by Eqs. 2.24-27 that builds on the virtues of the previous nonlinear models. As in the previous models, the initial growth rate is defined to be the linear growth rate when $kh_o^- \ll 1$ and it describes most of the compressible effects. However, for $kh_o^- \gg 1$, this must be reduced by nonlinear effects which we describe by the Pade' approximant of VD. Our model then has terms $\propto \tau$ designed to capture the spike acceleration and its explicit dependence on A^- and kh_o^- . In practical terms, our model is intermediate between the SEA model, which has no explicit dependence on kh_o^- , and the ZS model which has a somewhat unphysical dependence on kh_o^- . Finally, our model has a term $\propto \tau^2$ in the denominator in order to capture the expected and observed asymptotic velocity $\propto \lambda/t$. However, the coefficient of this term is found to be $F_{bu/sp} = 1 \pm |A|$ rather than that calculated by OG (Eq. 2.10). Our model compares much more favorably with the simulations over a wider range of parameters than the previous MIK, SEA and ZS models. Our hope is that such empirical models concisely capture the essence of RM simulations and that they may guide more rigorous analysis.

We would like to thank A. Calder, K. Mikaelian, O. Sadot, A. L. Velikovich, and J. G. Wouchuck for many useful discussions and A. Dhotre for assistance with the simulations. The FLASH software used in this work was developed in part by the DOE-sponsored ASC/Alliance Center for Astrophysical Thermonuclear Flashes at the University of Chicago. The PARAMESH software was developed at the NASA Goddard Space Flight Center under the HPCC and ESTO/CT projects. This work was performed for the U. S. Department of Energy by Los Alamos National Laboratory under Contract No. DE-AC52-06NA2-5396.

Appendix A. Nonlinear impulsive model

In the spirit of Richtmyer [1], an impulsive model that may be applicable to large initial amplitude is constructed here by integrating the nonlinear equations of potential flow [28, 35, 37, 38] across the initial amplitude. Since the evolutionary equations of potential flow vary differently with Atwood number depending on the form of the velocity potential, we simplify this analysis by choosing $A = 1$. Furthermore, we assume that the RM growth is incompressible

such that $kh_o^- \sim kh_o$. With these approximations, the potential flow equations in a gravitational field g (e. g. Eq. 8 of ref. [35]) reduce to

$$(1 - kh) \frac{d^2 h}{dt^2} + k \left(\frac{dh}{dt} \right)^2 = gkh \quad (\text{A1})$$

At small amplitude, this reduces further to the Rayleigh-Taylor unstable form used by Richtmyer because the coefficient in the first term reduces to unity and the second term vanishes. Then, for an impulsive $g \sim U\delta(t)$, the remaining terms ($\frac{d^2 h}{dt^2}$ and gkh) are proportional to a delta-function $\delta(t)$ and can be integrated to yield an impulsive model like Eqs. 2.4-5. However, dh/dt in Eq. A.1 is not proportional to $\delta(t)$ and must be integrated across the impulse for a specified time. Here, we postulate that such a time is related to a transit time across the initial perturbation at a rate given by the interface velocity, namely, for $\delta t \sim 2h_o/U$. Integrating Eq. A1 over δt yields

$$(1 - kh_o) \left(\frac{dh}{dt} \right)_o + \frac{2kh_o}{U} \left(\frac{dh}{dt} \right)_o^2 = V_o \quad (\text{A2})$$

where $V_o \sim Ukh_o$. The initial growth rate in Eq. A2 is constant and is given by the quadratic solution

$$\frac{1}{V_o} \left(\frac{dh}{dt} \right)_o = \frac{(kh_o - 1) + \sqrt{(kh_o - 1)^2 + 8(kh_o)^2}}{4(kh_o)^2} \quad (\text{A3})$$

This constitutes our nonlinear impulsive model obtained in the spirit of Richtmyer for an incompressible flow at $A = 1$. The extension to a compressible flow for all A is discussed in Sec. 3c.

Table 1: Parameters associated with experiments in Figs. 3-6. The values in parenthesis are only estimates used in the associated FLASH simulations, which require M_i , A^- , γ_A , γ_B , and kh_o^- as input.

Experiment Reference	NOVA [22, 23]	Shock tube [30]	Shock tube [43]	Coil spring [45]
Parameter				
ρ_A	1.7 g/cc			0.87 g/cc
ρ_B	0.12 g/cc			1.2 g/cc
γ_A	(1.8)	1.4	1.4	(1.67)
γ_B	(1.45)	1.09	1.09	(1.67)
Mach	~ 10	1.3	1.27	(1.1)
W_i	50 $\mu\text{m/ns}$			
U	71 $\mu\text{m/ns}$		90 m/s	
W_t	90 $\mu\text{m/ns}$			
ρ_2	(2.2 g/cc)			
ρ_1	0.6 g/cc			
A^-	-0.87	(0.67)	0.66	0.16
A	-0.61	(0.71)	0.69	0.16
h_o^-	10 μm	2 mm	1.47 mm	3 mm
λ	100 μm	16-80 mm	35.5 mm	83 mm
kh_o^-	- 0.63	0.16-0.78	0.26	0.23
kh_o	0.26	0.12-0.62	0.17	0.22

Table 2: Simulation parameters for Figures 18 and 19 with $kh_o^- = 1$.

Case	(a)	(b)	(c)	(d)
Parameter				
A^-	0.15	0.5	0.87	0.98
γ_A	1.67	1.1	1.67	1.1
γ_B	1.67	1.1	1.67	1.1
M_i	1.1	1.02	1.1	1.02

References

1. R. D. Richtmyer, 'Taylor instability in shock acceleration of compressible fluids', *Com. Pure Appl. Math.* **13**, 297 (1960)
2. E. E. Meshkov, 'Instability of the interface of two gases accelerated by a shock', *Fluid Dyn.* **4**, 101 (1969)
3. S. Atzeni and J. Meyer-Ter-Vehn, **The Physics of Inertial Fusion**, Clarendon Press, Oxford, UK, 2004
4. R. Betti, C.D. Zhou, K.S. Anderson, L.J. Perkins W. Theobald, A.A. Soldov, 'Shock ignition of thermonuclear fuel with high areal density', *Phys Rev Lett* **98**, 155001 (07)
5. A. L. Velikovich, A.J.Schmitt, J.H.Gardner, N. Metzler, 'Feedout and Richtmyer-Meshkov instability at large density difference', *Phys Plasmas* **8**, 592 (2001)
6. W. S. Vogán, W.W. Anderson, M. Grover, J.E. Hammerberg, N.S.P. King, S.K. Lamoreaux, G. Macrum, K.B. Morley, P.A. Rigg, G.D. Stevens, W.D. Turley, L.R. Veaser, W.T. Buttler, 'Piezoelectric characterization of ejecta from shocked tin surfaces' *J. App. Phys.* **98**, 113508 (2005)
7. M.B. Zellner, M. Grover, J.E. Hammerberg, R.S. Hixson, A.W. Obst, R.T. Olson, J.R. Payton, P. Rigg, N. Routley, G. Stevens, D. Turley, W. Vogán-McNeil, W.T. Buttler, 'Probing the underlying physics of ejecta production', *J. Appl. Phys.* **103**, 123502 (2008)
8. Guy Dimonte and Robert Tipton, 'K-L turbulence model for the self-similar growth of the Rayleigh-Taylor and Richtmyer-Meshkov instabilities', *Phys Fluids* **18**, 85101 (2006)
9. Guy Dimonte and M. Schneider, 'Density ratio dependence of Rayleigh-Taylor mixing for sustained and impulsive acceleration histories', *Phys Fluids* **12**, 304 (2000)
10. U. Alon, J. Hecht, D. Ofer, D. Shvarts, 'Power laws and similarity of Rayleigh-Taylor and Richtmyer-Meshkov mixing fronts at all density ratios', *Phys Rev Lett* **74**, 534 (1995)
11. D. Oron, L. Arazi, D. Kartoon, A. Rikanati, U. Alon, D. Shvarts, 'Dimensionality dependence of the Rayleigh-Taylor and Richtmyer-Meshkov instability late-time scaling laws', *Phys Plasmas* **8**, 2883 (2001)
12. Y. Yang, Q. Zhang and D. H. Sharp, 'Small amplitude theory of Richtmyer-Meshkov instability', *Phys Fluids* **6**, 1856 (1994)
13. K. M. Meyer and P. J. Blewett, 'Numerical investigation of the stability of a shock-accelerated interface between two fluids', *Phys Fluids* **15**, 753 (1972)
14. M. Vandenboomgaerde, C. Mugler and S. Gauthier, 'Impulsive model for the Richtmyer-Meshkov instability', *Phys Rev E* **58**, 1874 (1998)

15. Karnig O. Mikaelian, 'Freeze-out and the effect of compressibility in the Richtmyer-Meshkov instability', *Phys Fluids* **6**, 356 (1994)
16. Gary Fraley, 'Rayleigh-Taylor stability for a normal shock-density discontinuity interaction', *Phys Fluids* **29**, 376 (1986)
17. J. G. Wouchuck and K. Nishihara, 'Asymptotic growth in the linear Richtmyer-Meshkov instability', *Phys Plasmas* **4**, 1028 (1997)
18. J. G. Wouchuck, 'Growth rate of the Richtmyer-Meshkov instability when a shock is reflected', *Phys Rev E* **63**, 56303 (2001)
19. J. G. Wouchuck, 'Growth rate of the Richtmyer-Meshkov instability when a rarefaction is reflected', *Phys Plasmas* **8**, 2890 (2001)
20. A. N. Aleshin, E.V. Lazareva, S.G. Zaitsev, V.B. Rozanov, E.G. Gamali, I.G. Lebo, 'Linear, nonlinear and transient stages in the development of the Richtmyer-Meshkov instability', *Sov Phys Dokl* **35**, 159 (1990)
21. A. N. Aleshin, E.V. Lazareva, E.I. Chebotareva, S.V. Sergeev, S.G. Zaytsev, 'Investigation of Richtmyer-Meshkov instability induced by the incident and reflected shock waves', *Proc Sixth Int Workshop Phys Comp Turb Mix, Marseille, 1997*, edited by G. Jourdan and L. Houas (IUSTI Universite de Provence, France, 1997), p. 1
22. Guy Dimonte and Bruce Remington, 'Richtmyer-Meshkov experiments on the NOVA laser at high compression', *Phys Rev Lett* **70**, 1806 (1993)
23. Guy Dimonte, C. Eric Frerking, M. Schneider, B. Remington, 'Richtmyer-Meshkov instability with strong radiatively driven shocks', *Phys Plasmas* **3**, 614 (1996)
24. A. Dhotre, P. Ramaprabhu and Guy Dimonte, 'A detailed numerical investigation of the single-mode Richtmyer-Meshkov instability', *Bull Am Phys Soc* **53**, 157 (2009)
25. Q. Zhang and S.I. Sohn, 'An analytical nonlinear theory of Richtmyer-Meshkov instability', *Physics Lett A* **212**, 149 (1996)
26. Q. Zhang and S.I. Sohn, 'Nonlinear theory of unstable fluid mixing driven by shock wave', *Phys Fluids* **9**, 1106 (1997)
27. R. L. Holmes, Guy Dimonte, B. Fryxell, M.J. Gittings, J.W. Grove, M. Schneider, D. Sharp, A.L. Velikovich, R.P. Weaver, Q. Zhang, 'Richtmyer-Meshkov instability growth: experiment, simulation and theory', *J Fluid Mech* **389**, 55 (1999)
28. D. Layzer, 'On the instability of superposed fluids in a gravitational field', *Astrophys J* **122**, 1 (1955)
29. A. L. Velikovich and Guy Dimonte, 'Nonlinear perturbation theory of the incompressible Richtmyer-Meshkov instability', *Phys Rev Lett* **76**, 3112 (1996)

30. O. Sadot, L Erez, U. Alon, D. Oron, L.A. Levin, G. Erez, G. Ben-Dor, D. Shvarts, 'Study of nonlinear evolution of single-mode and two-bubble interaction under Richtmyer-Meshkov instability', *Phys Rev Lett* **80**, 1654 (1998)
31. M. Vandenboomgaerde, S. Gauthier and C. Mugler, 'Nonlinear regime of a multimode Richtmyer-Meshkov instability: a simplified perturbation theory', *Phys Fluids* **14**, 1111 (2002)
32. C. Matsuoka, K. Nishihara and Y. Fukuda, 'Nonlinear evolution of an interface in the Richtmyer-Meshkov instability', *Phys Rev E* **67**, 36301 (2003); erratum, *ibid.* **68**, 29902 (2003)
33. O. A. Likhachev and J. W. Jacobs, 'A vortex model for Richtmyer-Meshkov instability accounting for finite Atwood number', *Phys Fluids* **17**, 31704 (05)
34. Qiang Zhang, 'Analytic solutions of Layzer-type approach to unstable interfacial fluid mixing', *Phys Rev Lett* **81**, 3391 (1998)
35. V. N. Goncharov, 'Analytical model of nonlinear, single-mode, classical Rayleigh-Taylor instability at arbitrary Atwood numbers', *Phys Rev Lett* **88**, 134502 (2002)
36. Karnig O. Mikaelian, 'Explicit expressions for the evolution of single-mode Rayleigh-Taylor and Richtmyer-Meshkov instabilities at arbitrary Atwood number', *Phys Rev E* **67**, 26319 (2003)
37. Sung-Ik Sohn, 'Simple potential-flow model of Rayleigh-Taylor and Richtmyer-Meshkov instabilities for all density ratios', *Phys Rev E* **67**, 26301 (2003)
38. Sung-Ik Sohn, 'Density dependence of a Zuzunov model for Rayleigh-Taylor bubble fronts', *Phys Rev E* **70**, 45301 (2004)
39. Karnig O. Mikaelian, 'Analytic approach to nonlinear Rayleigh-Taylor and Richtmyer-Meshkov instabilities', *Phys Rev Lett* **80**, 508 (1998)
40. Karnig O. Mikaelian, 'Limitations and failures of the Layzer model for hydrodynamic instabilities', *Phys Rev E* **78**, 15303 (2008)
41. A. Rikanati, D. Oron, O. Sadot and D. Shvarts, 'High initial amplitude and high Mach number effects on the evolution of the single-mode Richtmyer-Meshkov instability', *Phys Rev E* **67**, 26307 (2003)
42. S. G. Glendinning, J. Bolstad, D.G. Braun, M.J. Edwards, W.W. Hsing, B.F. Lasinski, H. Louis, J. Moreno, T.A. Peyser, B.A. Remington, H.F. Robey, E.J. Turano, C.P. Verdon, Y. Zhou, 'Effect of shock proximity in Richtmyer-Meshkov growth', *Phys Plasmas* **10**, 1931 (2003)
43. J. W. Jacobs and V. V. Krivets, 'Experiments on the late-time development of single-mode Richtmyer-Meshkov instability', *Phys Fluids* **17**, 34105 (2005)
44. C. Mariani, M Vandenboomgaerde, G Jourdan, D. Souffland, L. Houas, 'Investigation of the Richtmyer-Meshkov instability with stereolithographed interfaces', *Phys Rev Lett* **100**, 254503 (2008)

45. C. E. Niederhaus and J. W. Jacobs, 'Experimental study of the Richtmyer-Meshkov instability of incompressible fluids', *J. Fluid Mech* **485**, 243 (2003)
46. M. Latini, O. Schilling, W. S. Don, 'High-resolution simulations and modeling of reshocked single-mode Richtmyer-Meshkov instability: Comparison to experimental data and to amplitude growth model predictions', *Phys Fluids* **19**, 24104 (2007)
47. A. Calder, J Dursi, B Fryxell, T. Plewa, G. Weirs, T. Dupont, H. Robey, J. Knae, B. Remington, F. Timmes, Guy Dimonte, J. Hayes, M. Zingale, P. Drake, P. Ricker, J. Stone, K. Olson, 'Validating astrophysical simulation codes', *Computing Sci. & Eng.* **6**, 22 (2004)
48. O. Sadot (private communication, 2009)

Figures

Figure 1: Configuration and nomenclature for RM instability before and after the interaction of shock with material interface

Figure 2: Amplitudes and images at $t = 20$ ms for simulations of a representative case with $M_1 = 1.02$, $\gamma_A = \gamma_B = 1.1$, $A^- = 0.98$, $\lambda = 2.09$ cm and $kh_o^- = 1$. The numbers represent the number of zones per wavelength for each simulation.

Figure 3: Scaled amplitude vs scaled time for NOVA experiment, FLASH simulations (black line) and models due to SEA (green), MIK (blue), ZS (brown) and our Eq. 2.24-2.27. Nova data taken with face-on (circles) and side-on (diamonds) x-ray radiographs on many different shots.

Figure 4: Scaled average amplitude vs scaled time for Air/SF6 shock tube experiments of SEA (grey circles) and JACOBS (grey diamonds) with $M = 1.27$. The lines represent the FLASH simulations (black line) and models due to SEA (green), MIK (blue), ZS (brown) and our Eq. 2.24-2.27 for $k=0.177$, $kh_o^- = 1.47$, $kh_o = 0.26$

Figure 5: Scaled amplitude of bubbles and spikes vs scaled time for Air/SF6 shock tube experiments of SEA (grey circles) with $M_1 = 1.27$. The lines represent the FLASH simulations (black line) and models due to SEA (green), MIK (blue), ZS (brown) and our Eq. 2.24-2.27 for $kh_o = 0.26$

Figure 6: Scaled amplitude of bubbles and spikes vs scaled time for the incompressible experiments of NJ (grey diamonds). The lines represent the FLASH simulations (black line) and models due to SEA (green), MIK (blue), ZS (brown) and our Eq. 2.24-2.27 for $kh_o = 0.26$

Figure 7: Scaled velocity (a, b) and amplitude (c, d) for bubbles (b, d) and spikes (a, c) for $A^- = 0.98$ & $kh_o^- = 0.125$ (37). The lines represent the FLASH simulations (black line) and models due to SEA (green), MIK (blue), ZS (brown) and our Eq. 2.24-2.27.

Figure 8: Scaled velocity (a, b) and amplitude (c, d) for bubbles (b, d) and spikes (a, c) for $A^- = 0.98$ & $kh_o^- = 1$ (40). The lines represent the FLASH simulations (black line) and models due to SEA (green), MIK (blue), ZS (brown) and our Eq. 2.24-2.27.

Figure 9: Interface profiles at selected times for cases in Figs. 7 and 8 with $A^- = 0.98$ and $kh_o^- = 0.125$ (a) and 1 (b)

Figure 10: Scaled velocity (a, b) and amplitude (c, d) for bubbles (b, d) and spikes (a, c) for $A^- = 0.15$ & $kh_o^- = 0.125$ (22). The lines represent the FLASH simulations (black line) and models due to SEA (green), MIK (blue), ZS (brown) and our Eq. 2.24-2.27.

Figure 11: Scaled velocity (a, b) and amplitude (c, d) for bubbles (b, d) and spikes (a, c) for $A^- = 0.15$ & $kh_o^- = 1$ (23). The lines represent the FLASH simulations (black line) and models due to SEA (green), MIK (blue), ZS (brown) and our Eq. 2.24-2.27.

Figure 12: Interface profiles at selected times for cases in Figs. 10 and 11 with $A^- = 0.15$ and $kh_o^- = 0.125$ (a) and 1 (b)

Figure 13: Scaled velocity (a, b) and amplitude (c, d) for bubbles (b, d) and spikes (a, c) for $k h_o^- = 0.125$ and $A^- = 0.98$ (37 black), 0.94 (43 red), 0.88 (34 green), 0.75 (44 blue), 0.5 (45 brown) and 0.25 (46 magenta). Solid lines are from FLASH simulations and dashed lines are our model Eq. 2.24-2.27.

Figure 14: Peak spike velocity taken from Fig. 13 vs Atwood number for $k h_o^- = 0.125$. Black line with diamonds are FLASH simulations and colored lines are SEA (green), MIK (blue), ZS (brown) and our model Eq. 2.24-2.27 (red). The magenta point is due to Zhang (Eq. 2.11) at $A^- = 1$.

Figure 15: Scaled velocity (a, b) and amplitude (c, d) for bubbles (b, d) and spikes (a, c) for $A^- = 0.98$ and $k h_o^- = 0.125$ (black), 0.25 (red), 0.5 (green), 1 (blue), 2 (brown), and 4 (magenta)(37-42). Solid lines are from FLASH simulations and dashed lines are our model Eq. 2.24-2.27.

Figure 16: Peak spike velocity taken from Fig. 15 vs $k h_o^-$ at $A^- = 0.98$. Black line with diamonds are FLASH simulations and colored lines are SEA (green), MIK (blue), ZS (brown) and our model Eq. 2.24-2.27 (red). The magenta point is due to Zhang (Eq. 2.11) at $A^- = 1$.

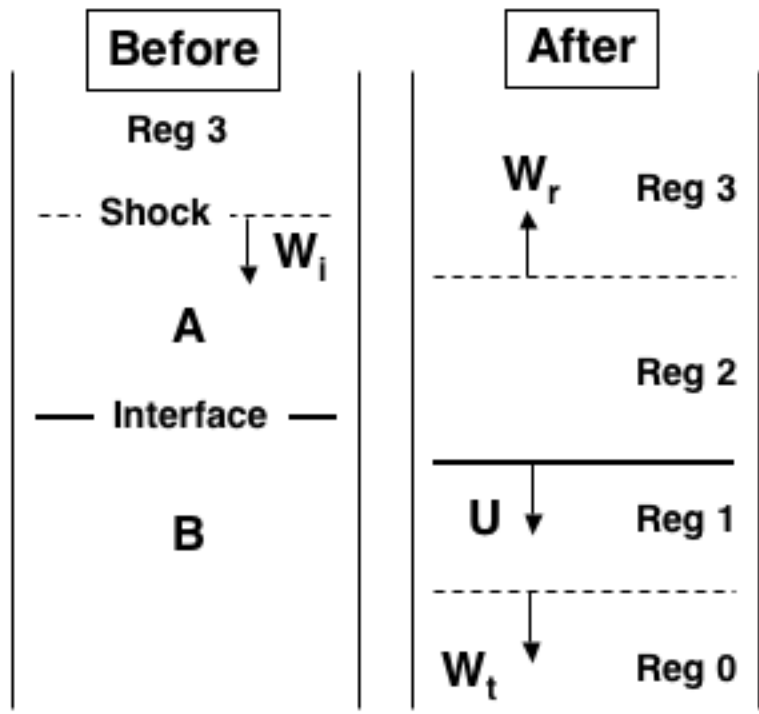
Figure 17: Scaled velocity (a, b) and amplitude (c, d) for bubbles (b, d) and spikes (a, c) for $A^- = 0.15$ and $k h_o^- = 0.125$ (black), 0.25 (red), 0.5 (green), 1 (blue), 2 (brown), and 4 (magenta)(22-24a). Solid lines are from FLASH simulations and dashed lines are our model Eq. 2.24-2.27.

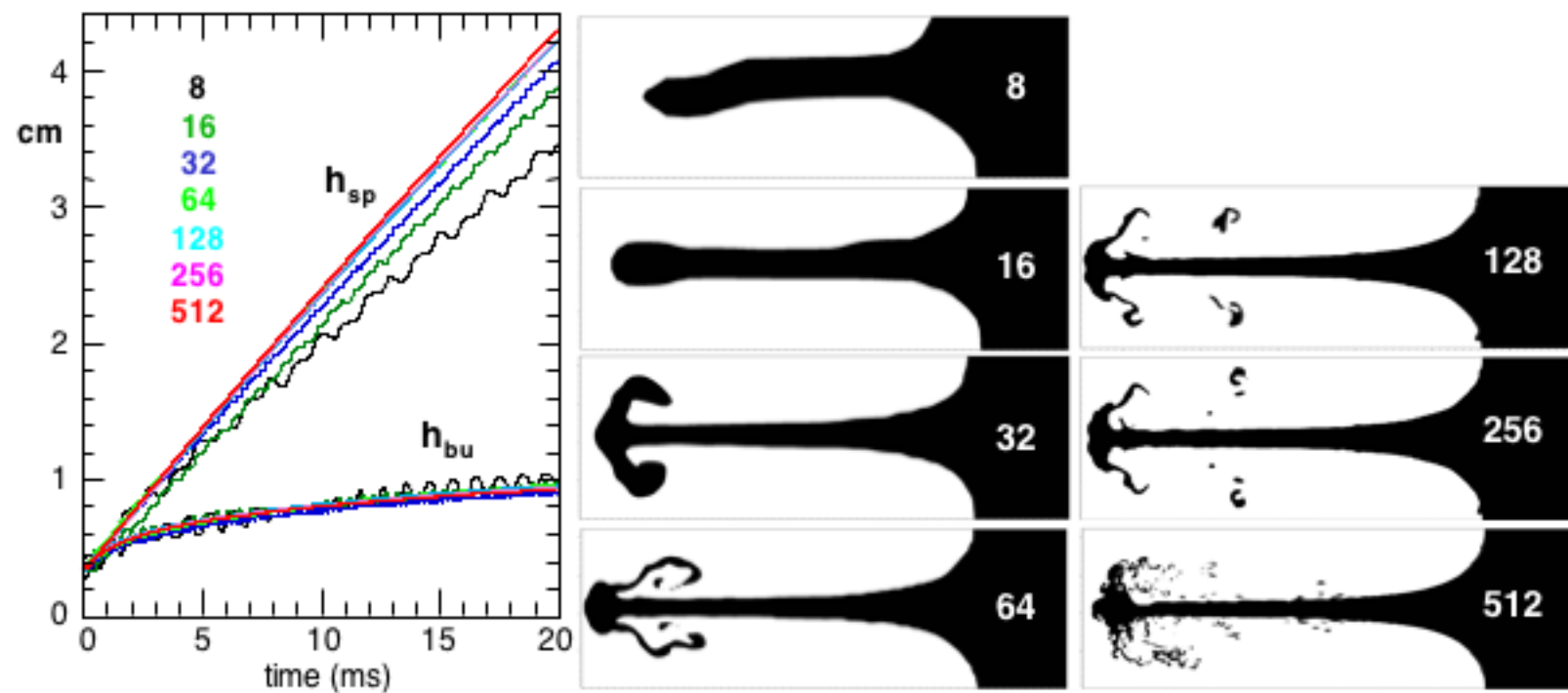
Figure 18: Scaled velocity of bubbles vs scaled time to asymptotic values for $k h_o^- = 1$ at $A^- = 0.15$ (23), 0.5 (45a), 0.87 (26) and 0.98 (40). Black line with diamonds are FLASH simulations and colored lines are SEA (green), MIK (blue), ZS (brown) and our model Eq. 2.24-2.27 (red). Dashed black line shows slope of $1/t$ expected from potential flow. Conditions for each case are summarized in Table 2.

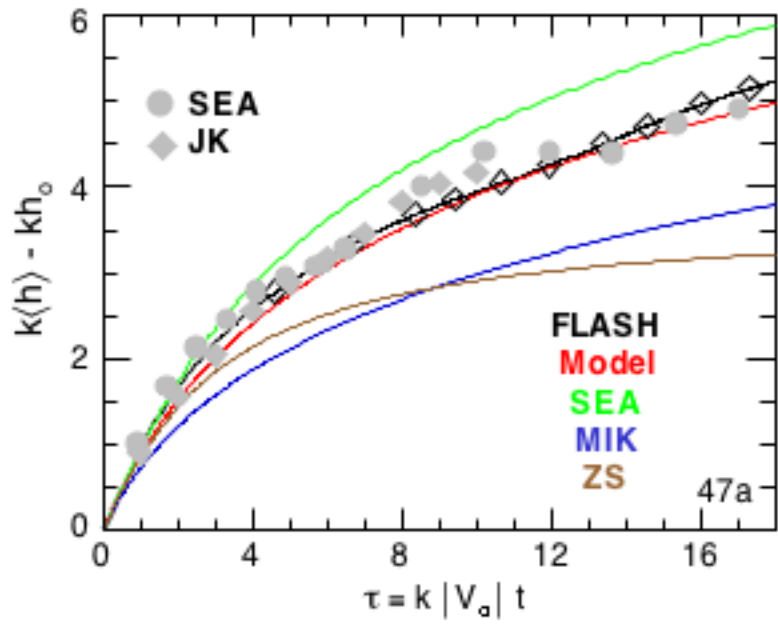
Figure 19: Scaled velocity of spikes vs scaled time to asymptotic values for $k h_o^- = 1$ at $A^- = 0.15$ (23), 0.5 (45a), 0.87 (26) and 0.98 (40). Black line with diamonds are FLASH simulations and colored lines are SEA (green), MIK (blue), ZS (brown) and our model Eq. 2.24-2.27 (red). Dashed black line shows slope of $1/t$ expected from potential flow. Conditions for each case are summarized in Table 2.

Figure 20: Diamonds are initial velocity required to fit simulation result to our model (Eq. 2.24-2.27) scaled to linear growth rate (from simulations with $k h_o^- = 0.125$) vs initial amplitude. Solid line is from Pade' approximant of VD and dashed line is our approximation Eq. 2.27.

Figure 21: Initial growth rate scaled by the linear growth rate vs $k h_o^-$. Points are from SEA (circles) [30], Aleshin, et al (diamonds) [20, 21] and Dimonte, et al (squares) [22, 23]. Solid black line is Pade' approximant of VD and dashed (dotted) black line is our model Eq. 2.24-2.27 evaluated at $t = 1$ for $A^- = 1$ (0). The red line is given by our nonlinear impulsive model Eq. 3.3.







47a

